PARTICLE IMAGE VELOCIMETRY MEASUREMENTS OF THE MEAN FLOW CHARACTERISTICS IN A BUBBLE PLUME

(EM/2005/024144)

By Dong-Guan Seol[1], Tirtharaj Bhaumik[2], Christian Bergmann[3], and Scott A. Socolofsky[4], Member ASCE

Keywords: bubbles, plumes, two phase flow, entrainment, laboratory tests, experimental data, dimensional analysis, velocity distribution

Abstract: A direct measurement method for the velocity field in multiphase flows using the particle image velocimetry (PIV) and particle tracking velocimetry (PTV) methods is developed to study the flow characteristics of an unbounded bubble plume in quiescent, unstratified ambient conditions. A single camera is used to obtain images containing both bubbles and fluid tracer particles. Using gray-scale thresholding, phase-separated images of the bubbles are produced, and bubble velocities are obtained from these images using the standard PTV method. Regular PIV is applied to the mixed fluid images, and bubble vectors are removed using a velocity threshold and vector median filter that is calibrated to the PTV result. From the separate velocity fields, the time-averaged flow characteristics of a bubble plume are studied. Gaussian velocity profiles match the entrained fluid velocity, and top-

---

[1] Research Assistant, Dept. Civil Engrg., Ocean Engrg. Div., Texas A&M Univ., M.S. 3136, College Station, TX 77843-3136. E-mail: seoldg@tamu.edu

[2] Research Assistant, Dept. Civil Engrg., Ocean Engrg. Div., Texas A&M Univ., M.S. 3136, College Station, TX 77843-3136. E-mail: tirtharaj@tamu.edu

[3] Visiting Scholar, Dept. Civil Engrg., Ocean Engrg. Div., Texas A&M Univ., M.S. 3136, College Station, TX 77843-3136. Now at Institute for Hydromechanics, University of Karlsruhe, 76128 - Karlsruhe, Germany. E-mail: bergmann@ifh.uni-karlsruhe.de

[4] Corresponding Author: Assistant Professor, Dept. Civil Engrg., Ocean Engrg. Div., Texas A&M Univ., M.S. 3136, College Station, TX 77843-3136. E-mail: socolofs@tamu.edu

hat velocity profiles match the bubble velocity. Time-averaged values are also presented of velocity, plume width, entrained fluid volume flux, and void fraction as a function of height. From these data, the entrainment coefficient for the entrained ambient fluid is calculated and lies between 0.08 near the plume source and 0.05 in the upper reaches. The results for the entrainment coefficient, together with those from the literature, are correlated to a non-dimensional velocity, given by the ratio of the bubble slip velocity u_s to a characteristic velocity in the plume $(B/z)^{1/3}$, where B is the kinematic buoyancy flux and z is the height above the source.

INTRODUCTION

Multiphase flows occur in a wide range of engineered and natural systems. In contrast to many chemical and environmental engineering applications, where the multiphase flow fills the domain of interest (e.g. bubble columns, chemical reactors), many environmental applications involve unbounded plumes issuing from nearly point-source conditions. These applications include bubble plumes for reservoir aeration or destratification (e.g. McDougall 1978, Wüest et al. 1992, Asaeda & Imberger 1993, Lemckert & Imberger 1993), oil and natural gas plumes for assessing the fate of oil released from accidental undersea oil-well blowouts (e.g. Yapa et al. 1999, Socolofsky & Adams 2002, Socolofsky & Adams 2003), and the direct injection of liquid CO_2 in the deep ocean as a means to mitigate atmospheric build-up of greenhouse gases (e.g. Caulfield et al. 1997, Socolofsky et al. 2002, Socolofsky & Adams 2005). These later cases are commonly approximated as self-similar, axially-symmetric plumes, and integral plume models of various complexity have been applied to evaluate their behavior (e.g. McDougall 1978, Wüest et al. 1992, Asaeda & Imberger 1993). While several important characteristics of the axially symmetric two-phase flow have been measured, such as entrained fluid volume flux and plume width, it remains to measure detailed, full-field velocity for the unbounded case. Thus, we present laboratory experiments using non-intrusive measurement technology that capture instantaneous and time-averaged full-field velocity information for the continuous and dispersed phases of an unbounded bubble plume in quiescent, unstratified ambient conditions. These measurements are important to quantify the entrainment coefficient needed by integral models and to evaluate the interactions between the dispersed phase and the entrained ambient fluid.

Common image velocimetry methods, such as particle image velocimetry (PIV) and particle tracking velocimetry (PTV), have been developed and applied by other researchers to understand the flow characteristics and mixing properties of various two-phase flows (Gui & Merzkirch 1996, Gui et al. 1997, Delnoij et al. 1999, Brücker 2000, Deen 2001, Lindken & Merzkirch 2002). The major advantage of these image velocimetry methods is their ability to capture instantaneous velocity field information non-invasively. Both PIV and PTV employ similar data processing techniques, which include double-exposed or double-frame images of tracer particles illuminated by successively pulsed laser sheets and calculate the velocity by dividing the displacement of seeded particles with the time interval between laser pulses (Oakley et al. 1997). The difficulty in multiphase flows lies in the fact that the bubble phase and liquid phase exist together in the flow.

Thus, the challenge in applying PIV or PTV to multiphase flows is in separating the tracer particles tracking the entrained continuous phase from the dispersed phase particles, droplets, or bubbles. Previous methods to separate the gaseous and liquid phases to apply PIV or PTV can be summarized according to which stage in the analysis the phase separation has been made. First, at the image capture stage, two separate images can be generated for bubbles and fluorescent tracer particles using optical separation methods with two cameras and an optical filter (Sridhar et al. 1991, Hilgers et al. 1995, Deen 2001). PIV and PTV methods can be applied to the separated bubble and fluorescent particles images to obtain phase-separated velocity fields. Second, a single image can be captured for both phases simultaneously and then image processing techniques can be used to identify the bubble signature and separate the phases before applying PIV or PTV (Gui & Merzkirch 1996, Gui et al. 1997, Delnoij et al. 1999, Brücker 2000, Grota & Strauß 2000, Kiger & Pan 2000, Deen et al. 2002). Gui & Merzkirch (1996) and Gui et al. (1997) used the size difference between bubbles and tracer particles, and Sakakibara et al. (1996) made use of gray-scale intensity differences to discriminate the two phases. Other methods include applying a median filter (Kiger & Pan 2000), edge detection algorithms (Brücker 2000), or digital masking techniques (Lindken et al. 1999, Gui & Merzkirch 1996, Grota & Strauß 2000). In each case, the bubbles and continuous phase tracer particles are separated into two images before PIV or PTV analysis. Third, the bubble signature can be removed during the PIV or PTV analysis using ensemble correlation methods based on the slip velocity (Delnoij et al. 1999, Deen et al. 2002). The bubble phase and fluid phase have different correlation peaks in the correlation field, so that they can be separated based on their velocity, the higher velocities being attributed to the bubbles. Among these techniques, the optical phase separation method is preferred; however, it requires the use of two cameras per interrogation window and expensive fluorescent tracer particles. The single-image phase separation methods are also successful, but require computationally expensive image processing methods or customized PIV and PTV algorithms.

In contrast to these methods, we propose a simple, inexpensive method for phase separation that uses standard tools available in most PIV software. The primary difference in our method is that the phase discrimination is made after processing the mixed-fluid PIV images; whereas, previous methods remove the bubbles before PIV processing. In our method, single, mixed-fluid images are captured using one camera. A pixel intensity threshold is used to obtain images of the bubbles only. PTV is applied to these images, yielding the bubble velocity information. Regular PIV is then applied to the unprocessed mixed-fluid images. The velocity field obtained from PIV, therefore, contains vectors for both the bubbles and the entrained fluid. The bubble vectors are subsequently removed using a velocity threshold and median filter technique. The parameters of the median filter are calibrated so that the extracted PIV bubble vectors match the results of the PTV analysis. The remaining vectors constitute the entrained fluid velocity field. In this way, phase separated results are obtained using standard PIV and PTV software. These results are then used to study the behavior of the two-phase plume.

The main goal of this study is to apply simple PIV and PTV analysis to an unbounded bubble plume to obtain the mean-flow characteristics of the plume. The Methods section describes the experimental set-up and details the procedures for our phase separation algorithm. The Results and Discussion section first presents the mean flow characteristics of the bubble and fluid phases obtained from the laboratory measurements and then compares our results for the entrainment coefficient to those of other researchers. From these data, the entrainment coefficient in two-phase plumes is shown to depend on a dimensionless slip velocity.

METHODS

The experiments were conducted in the Hydromechanics Laboratory of the Ocean Engineering Program at Texas A&M University. Figure 1 shows the set up for the experiments. A Plexiglas tank with dimension of 38×38×80 cm was used in the experiments. The air was injected from an aquarium air diffuser with stone diameter of 1.4 cm, which was fixed to the tank bottom. The characteristic diameter of bubbles generated from the airstone diffuser was 1.5 to 2.0 mm. A needle valve and gas mass flow meter (Alborg GFM 171) enabled precise control of the air flow rate from the air source. The air flow rates in the experiments were 0.5, 1.0, and 1.5 l/min at standard temperature and pressure (STP).

[FIG. 1 about here.]

The setup for the experiments was typical of a PIV study. An Nd:YAG double-pulsed laser (wave length 532 nm, 320 mJ/pulse) was used to generate a light sheet using a spherical lens. The light sheet thickness was adjusted to 3 mm in order to increase the possibility of capturing wobbling bubbles. Due to availability, two different kinds of CCD cameras, a FlowMaster 3S camera (12-bit intensity depth with 1280×1024 resolution) and two Basler cameras (10-bit intensity depth with 1004×1004 resolution) were used. The cameras were positioned at different heights to take images of the whole plume from a height of 8 cm above the diffuser (the beginning of the zone of established flow) to a maximum height of 60 cm above the diffuser. The fields of view of each camera were 21×18 cm for the FlowMaster 3S camera at the bottom and 18×18 cm for the two Basler cameras at the middle and top of the plume, each field of view having 1 cm of overlap. In order to synchronize the cameras and laser, a careful timing control scheme was adopted. The three cameras and the pulse generator that controlled the laser (500A by Berkeley Nucleonics Corporation) were triggered using LabVIEW and a National Instruments PCI-6713 analog signal output board (12-bit × 8 channels).

Velocity fields are obtained for the entrained fluid and bubbles from a single set of images. As the bubbles released from the airstone diffuser rise with a velocity of approximately 40 cm/s (Socolofsky 2001), the time interval between image pairs was chosen as 4 ms, in which the average bubble displacement was around 10 pixels. Non-fluorescent tracer particles were added to the water to track the entrained fluid; the particles were white polyamide spheres with a characteristics diameter of 50 μm. Due to their different diameter and light scattering characteristics, the bubbles and the seeding tracer particles have different gray-scale values in the captured images. Specifically, the gray-scale intensities of the seeding tracer particles ranged from 1000 to 2000 in the high-resolution camera and from 200 to 400 in the low-resolution cameras; whereas, the gray-scale intensity of the bubbles was controlled to have nearly saturation intensity in both cameras (4095 in the high-resolution camera and 1024 in the low-resolution cameras). The lower light intensity of the seeding tracer particles is equivalent to using a camera with lower bit depth (Raffel et al. 1998). Because we are using 10 and 12 bit cameras, the particles were always imaged with a greater than 8 bit intensity depth so that the error in the particle displacement predicted by PIV is between 0.1 and 0.3 pixels, which is very near the limit of the resolution of the PIV method at higher bit depth. As a result, we do not expect a significant difference in the uncertainty for velocity vectors obtained for the bubbles or the entrained fluid from the mixed-fluid images.

Although most of the bubble signature is bright, shadow effects cause some regions of the bubble signature to be rather dark. As a result, it was not possible to completely remove the bubble signature from the mixed fluid images purely on account of their gray-scale intensity. As discussed in the introduction, several images processing methods have been described in the literature to remove the bubble signature from the images before PIV or PTV processing. In the following, we describe an alternate phase separation method which is applied after the PIV and PTV processing.

Phase Separation Method

Because images are obtained that contain both the bubbles and the entrained fluid tracer particles, a data analysis method is required to obtain phase-separated results.

The bubble velocity field is obtained using the standard PTV method applied to an image containing only the bubble signature. The bubble-only image is obtained by selecting pixels from the mixed fluid image that lie above a threshold intensity value. Since there is nonuniformity in the laser intensity from top to bottom and since the opposite side of a bubble plume from the side the laser light enters is darker, some bubbles in the raw image have lower gray-scale intensity than the saturation intensity. Therefore, the threshold values are carefully chosen to ensure that most of the bubbles are extracted. The gray-scale values of 3000 for the high resolution camera and 500 for the low resolution camera were chosen as thresholds. Figure 2

[FIG. 2 about here.]

shows an example portion of the mixed fluid image (a) and the separated bubble image (b) after applying the threshold value. After thresholding, the true bubble velocities are obtained by applying PTV to the extracted bubble images.

The velocity field for the entrained fluid is obtained by post-processing of the mixed fluid PIV results. The PIV method detects the displacement of a particle in a divided small interrogation window. First, the standard PIV method is applied to the mixed fluid images with the interrogation areas chosen as 32×32 pixels at the first pass and 16×16 pixels at the second pass with an overlap of 50%. To obtain the entrained fluid velocity vector field, the unwanted bubble vectors were removed in a first, rough pass by specifying an allowable velocity range for the entrained fluid and in a second, final pass by applying the vector median filter to remove the remaining bubble vectors. In this study, the allowable maximum vertical velocity of the entrained fluid was set to 30 cm/s and the maximum horizontal velocity to 20 cm/s. The remaining bubble vectors were then filtered out using the vector median filter. The median filter is a nonlinear filter to remove outlier vectors (Westerweel 1994). The median filter sorts a specified number of neighboring vectors into ascending order and finds the median value of the velocities. Then, it determines the range of allowable vectors as follows:

$$U_{med} - fU_{rms} \leq U \leq U_{med} + fU_{rms} \tag{1}$$

where U denotes the allowed vector components in the x- and y-direction, and U_{med} and U_{rms}

denote the median vector and standard deviation of all neighboring vectors, respectively (LaVision GmbH 2002). The parameter f for the median filter is specified to adjust the allowable vector range. The parameter f and the number of neighboring vectors taken into account are specified by careful visual examination of the raw image and velocity vector field. A sample median filtered vector map is shown in Figure 3.

[FIG. 3 about here.]

The parameter values for the median filter were determined by examining the overlapped vector map with the raw image and selecting their values to remove all the bubble velocity vectors from the raw vector map. The results of this phase separation are verified by comparing the extracted vectors to the PTV analysis results. This is presented later in the Results and Discussion section.

Figure 4

[FIG. 4 about here.]

shows the complete procedure to obtain phase-separated vector maps from a raw image. Figure 4(a) shows the raw image from the experiments. After applying PIV to this raw image, the fluid-phase velocity vector map (b) and the bubble-phase velocity vector map (c) can be separated using a velocity threshold and median filter as mentioned above. The bubble velocity vector map from the PTV analysis (d) is shown for comparison.

Limitations

We first point out that our phase discrimination method is not intended to be better than the optical phase separation methods using fluorescent particles and multiple cameras or image processing techniques that remove the bubble signature before PIV processing. Instead, we are proposing a simpler method that works adequately for the measurements we seek, which are of the mean flow field in dilute bubble plumes.

The phase-discrimination method proposed here has some limitations. First, the dispersed phase must have large bubbles or droplets compared to the size of the entrained fluid PIV tracer particles. This is required for two reasons: (1) the correlation peak for the bubble signature in an individual interrogation window must be much greater than that for the tracer particles and (2) there must be a significant slip velocity between the dispersed and continuous phase for the median filter to accurately identify bubble velocities. Figure 5 shows a sample PIV interrogation window in our experiments. For air, bubble sizes above 2 mm satisfy the requirements of our method given our experimental set-up. Second, the bubble concentration must be low enough that a significant number of entrained fluid vectors are obtained within the bubble plume core, otherwise, no information on the entrained fluid will be collected. In our set up, the bubble flow rate of 1.5 l/min had a void fraction of 3% near the bottom of the plume which was near the limit of the applicability of our method. For higher void fraction, a smaller field of view and greater magnification would have been required. Third, because continuous phase velocity vectors immediately behind the bubbles are similar to the velocity of the bubbles, our method treats them as a bubble velocity vector. As a result, the entrained fluid velocity has some bias toward lower than actual velocity. This error is unavoidable in this method. However, environmental applications deal with dilute plumes where the void fraction is well below 5%. Thus, the great majority of fluid is not

[FIG. 5 about here.]

traveling in the immediate wake of the bubbles and the results of our method should be adequate to capture the mean flow characteristics in dilute bubble plumes.

Data Analysis

To obtain mean velocity profiles for the dispersed and continuous phases, the instantaneous velocity data were processed to remove the plume wandering effect and then time averaged. Plume wandering is the tendency for the plume centerline to meander slowly during an experiment, which can be significant in a closed, unstratified tank. To remove the plume wandering effect in the data, we had to identify the instantaneous plume centerline and then shift the data so that the centerline was moved to the middle of the tank. Because of the patchiness of the phase-separated data, a spatial average was applied to obtain the instantaneous velocity averaged over ten rows of PIV vectors (about 2 cm vertical extent of the plume). A Gaussian profile was then fit to the filtered data and the center of the Gaussian profile was taken as the instantaneous plume centerline. The raw velocity data were finally shifted so that the plume wandering was removed. In shifting the data, plume wandering was not severe enough that the plume interacted with the walls of the tank. After the instantaneous data were shifted, time-average velocity fields were obtained by averaging 600 double frames of velocity data (150 seconds).

From the time-averaged velocity fields, the velocity profiles for the bubble phase and fluid phase can be found. From the data, the fluid velocity profile follows a Gaussian distribution described by

$$U(z,r) = U_m(z) \exp\left(-\left(r/b\right)^2\right) \tag{2}$$

where b is the plume width, and $U_m(z)$ is the centerline velocity of the fluid phase velocity profile; z and r denote the vertical and horizontal direction coordinates, respectively. The parameters of the Gaussian curve, b and U_m, are determined by non-linear least-squares regression applied to the time-averaged velocity field information. These centerline values along the plume height provide the fluid volume flux and momentum flux. Moreover, the bubble velocity profiles more closely resemble a top-hat profile, and the curve fitted to the data is the reverse of a shallow water wake profile suggested by Monkewitz (1988), given by

$$U(z,r) = \frac{U_b(z)}{1 + \sinh^{2\beta}(r/b_b)} \tag{3}$$

where $U_b(z)$ and b_b are the maximum value and width of the bubble velocity profile. These values are also determined from non-linear least-squares regression in the same manner as for the fluid phase. β is a parameter that adjusts the flatness of the central part of the profile. Taking $\beta = 1$ gives a profile very similar to the Gaussian profile. In this study, $\beta = 3$ was chosen as the best match to the measured data.

RESULTS AND DISCUSSION

Experiments were performed for bubble flow rates of 0.5, 1.0, and 1.5 l/min at STP. The results of these experiments are discussed in the following.

Velocity Profiles and Verification of Phase Separation Method

To verify the phase separation method used to remove the bubble velocity vectors from the mixed fluid PIV results, the PIV data are compared to the PTV data for the bubble velocity. Figure 6(a) and (b)

[FIG. 6 about here.]

show the time-averaged velocity profiles for the bubble phase at different heights. The bubble velocity data were fitted to the Monkewitz curve (Eq. (3)) as suggested in the previous section. The profiles of the rise velocity resemble a top-hat profile with a maximum velocity around 40 cm/s and zero over the outside of the plume.

In Figure 6(a) and (b) the data from the PTV analysis (×) are plotted together with the bubble data removed from the PIV results using the median filter (○). The fitted value of f for the median filter varied between 1 to 1.5 to obtain the best fit. The number of neighboring vectors for the median filtering was 4. From the figure, it is confirmed that the extracted bubble velocity data from the PIV are in agreement with the bubble velocity data from the PTV. We also conclude that the remaining continuous phase vectors in the PIV data do not include the bubble signature.

Figure 6(c) and (d) illustrates the average velocity profile of the fluid phase at two heights for the flowrate of 0.5 l/min. The Gaussian curve fit to the entrained fluid shows good agreement with the measured data. According to these profiles, water is carried upward with a maximum velocity of 20 cm/s near the center of the profile. The fluid phase velocity profiles also show plume-like behavior. In other words, the velocity profiles become wider as they go to a higher part of the plume, while the maximum velocity gets slower.

Figure 7

[FIG. 7 about here.]

shows the normalized entrained fluid velocities at different heights. The fluid velocity was normalized with the centerline velocity, and the plume radius was normalized with plume width obtained from the best-fit Gaussian curves. The data in the figure show that the Gaussian velocity profile matches the data well throughout the zone of established flow.

Mean Flow Characteristics

From the fitted Gaussian and Monkewitz curves to the time-averaged velocity field data, average flow characteristics are obtained. Figure 8

[FIG. 8 about here.]

illustrates the non-dimensionalized centerline velocity and plume width for the bubble phase (a and c) and the fluid phase (b and d). To compare the results for different gas flow rates, the centerline velocity and plume width have been nondimensionalized by the height in the plume z and the kinematic buoyancy flux B, which is defined as

$$B = Q_0 \frac{\Delta\rho}{\rho_w} \frac{H_A}{H_T} g \tag{4}$$

where Q_0 is the volume flow rate of air bubbles at STP, H_A is the atmospheric pressure head (10.4 m), and $H_T = H_A + h$ is the static pressure head at the diffuser, where h is the depth of the diffuser. $\Delta\rho$ is the density difference between fresh water ($\rho_w = 1000$ kg/m^3) and air ($\rho_a = 1.4$ kg/m^3). Then, the non-dimensional parameters for a simple bubble plume can be given by dimensionless centerline velocity U_m^*, dimensionless height from the release point

z^*, and dimensionless plume width b^* as follows:

$$U_m^* = \frac{U_m(z)}{(B/z)^{1/3}} \tag{5}$$

$$z^* = \frac{z}{H_T} \tag{6}$$

$$b^* = \frac{b(z)}{z} \tag{7}$$

These non-dimensional combinations are the common choice for presenting plume data.

As shown in Figure 8(a), the non-dimensional centerline velocity for the bubble phase steadily increases with plume height, but also with bubble flow rate. The effective bubble slip velocity (velocity difference between a bubble and the mean flow of the surrounding water) varies with bubble size and bubble concentration (Schlüter & Räbiger 1998) and increases with increasing air flow rate in our experiments. Each air flow rate results in a slightly different bubble size and group swarm characteristics; hence, each air flow rate has a different characteristic bubble slip velocity. The dimensional combination $(B/z)^{1/3}$ is a characteristic velocity of the entrained ambient fluid that does not reflect the dependence of slip velocity on bubble flow rate. Thus, we would not have expected a collapse of the data in plot (a) and the lack of data collapse is due to the variable effective slip velocity across experiments.

The other profiles in Figure 8 do show good collapse of the data. For all flow rates, the non-dimensional centerline velocities of the fluid phase (plot b) become steady above 0.035 in the non-dimensional plume height units. For both the bubbles and the entrained fluid, the variation of the non-dimensional plume width is steep in the lower part of the plume and shallower in the upper part of the plume. This variation of plume width with height shows that the bubble plume does not strictly follow self-similarity.

Based on the Gaussian profiles of the fluid velocity, the volume flux of the fluid phase can be calculated by integrating the fluid velocity profile curves. The volume flux of the plume water is then defined as

$$Q = \int_0^\infty 2\pi r(1 - C(z,r))u(z,r)dr \tag{8}$$

where $C(z, r)$ is the void fraction of air bubbles and $u(z, r)$ is the fluid velocity profile. For the experimental profiles, limits of the numerical integration were chosen as the half width of the tank; we also make the dilute plume assumption $(1 - C \approx 1)$. By dimensional analysis, the entrained fluid flow rate is nondimensionalized as follows

$$Q^* = \frac{Q}{(Bz^5)^{1/3}} \tag{9}$$

The calculated volume flux over the plume height is presented in Figure 9(a).

[FIG. 9 about here.]

The non-dimensional volume flux of the fluid phase decreases sharply at the beginning but becomes steady as it rises. For different flow rates, there is no significant difference in non-dimensional fluid volume flux with non-dimensional height. This graph shows that the volume flux of the fluid phase depends on the initial buoyancy flux and plume height rather than the slip velocity.

The void fraction in the plume can also be calculated by assuming isothermal expansion of the bubbles. Using the ideal gas law, the known bubble flow rate is set equal to the bubble flux assuming a Gaussian distribution of bubbles (typical of integral plume models). The void fraction C is then computed from

$$Q_b(z) = \frac{Q_0 H_A}{(H_T - z)} = \int_0^\infty 2\pi r C(z,r)(u(z,r) + u_s)dr = \pi b^2 C(z)\left(U_m(z) + u_s\right) \tag{10}$$

where $Q_b(z)$ is the gas volume flux at any given height, $C(z)$ is the void fraction, and u_s is the bubble slip velocity. The bubble slip velocity was estimated based on the mean equivalent bubble diameter. Here, the equivalent bubble diameter is defined as the diameter of a spherical bubble with the same volume as the ellipsoidal bubble in the raw images. The mean equivalent bubble diameters d_e in the experiments were extracted from the images as 1.51 mm, 1.71 mm, and 2.02 mm for 0.5 l/min, 1.0 l/min, and 1.5 l/min, respectively. The slip velocities for these bubble diameters were 16.76 cm/s, 18.26 cm/s, and 20.41 cm/s in tap water (Motarjemi & Jameson 1978). These velocities are in good agreement with the measured data. These values were used to calculate the void fraction as shown in Figure 9(b). The calculated void fraction ranges 1 to 1.8% at the bottom and 0.2 to 0.7 % at the top. These data verify the dilute plume assumption and also show that the void fraction is a function of bubble flow rate, which is to be expected.

Entrainment Coefficient

From the measured data, the effective entrainment coefficient α can be calculated by the relationship between the maximum mean velocity of the fluid phase and the volume flux into the plume (Milgram 1983), which is given by

$$\frac{dQ}{dz} = 2\pi b \alpha U_m \tag{11}$$

The gradient of volume flux was determined by fitting the volume flux data of Figure 9(a) to a smooth curve to eliminate the noise amplification that occurs when applying dQ/dz to the raw PIV data. Using the obtained volume flux gradient and centerline values, the entrainment coefficients were determined as shown in Figure 10.

[FIG. 10 about here.]

Until the non-dimensional water depth of 0.035, which is comparable with distance to 35 cm from the diffuser, the entrainment coefficient continuously decreases and lies in the range of 0.08 to 0.05. This agrees well with the pure plume value of 0.083 (Fischer et al. 1979). In this region, the plume behaves like a simple plume in an unbounded domain, and the non-constant entrainment coefficient value indicates that the plume is not strictly self-similar. Beyond this height, however, the entrainment coefficient grows abruptly up to 0.15 and then drops quickly near the water surface. This can be attributed to the water surface effect. In other words, after the plume hits the water surface, the plume fluid propagates outward from the plume center. This surface current causes a recirculation flow that influences the plume above $z^* = 0.035$. Hence, pure plume entrainment coefficients can only be inferred below the height of $z^* = 0.035$.

Milgram (1983) proposed the bubble Froude number as a scaling factor to provide a functional relationship between the entrainment coefficient and other local independent variables of a bubble plume. Using dimensional analysis, he found the bubble Froude number, which is the ratio of the mixing distance of bubble motions in the turbulence to the characteristic distance between bubbles, and is expressed as:

$$F_B = \left(\frac{Q_b^2}{g}\right)^{1/5} \frac{C^{1/3}\sqrt{g\Delta\rho}}{\sqrt{T}} \tag{12}$$

where T is the surface tension between an air bubble and water (0.072 N/m). Figure 11 shows the correlation of α with F_B for our data along with the data presented in Milgram (1983). F_B ranged in our experiments between 0.25 and 0.65, whereas Milgram compared to data with F_B between 1 and 45. Although Milgram's correlation indicates $\alpha \to 0$ as $F_B \to 0$, the low F_B data from our experiments predict a minimum threshold value of $\alpha = 0.05$ to 0.04, which is also consistent with Milgram's data. Hence, a better correlation is required for α at low F_B.

[FIG. 11 about here.]

In order that the effective entrainment coefficient for our three experiments can be collapsed to one regression curve, a relationship between the entrainment coefficient and the plume parameters was derived. Here, the independent plume parameters are B, z, and u_s. We use u_s as a single parameter that includes the effects of d_e, T, and $\Delta\rho$. Using our three independent parameters, the dimensionless slip velocity can be expressed as $u_s/(B/z)^{1/3}$. This parameter is the ratio of the slip velocity to a characteristic entrained fluid velocity $(B/z)^{1/3}$. Socolofsky & Adams (2002) used this ratio to predict when multiphase plumes in crossflow would loose their plume behavior due to downwind detrainment, and this parameter is the analog of the non-dimensional slip velocity proposed by Socolofsky & Adams (2005) for a stratified ambient, $U_N = u_s/(BN)^{1/4}$, where N is the buoyancy frequency and $(BN)^{1/4}$ is a characteristic velocity. Then, the entrainment coefficient based on our experimental data below $z^* = 0.035$ gives the functional relationship

$$\alpha = \frac{B/u_s^3}{8.221z} + 0.0469 \tag{13}$$

Figure 12

[FIG. 12 about here.]

shows the relationship between the entrainment coefficient and the dimensionless slip velocity derived above. Entrainment coefficients measured by previous researchers (Kobus 1968, Fenneløp & Sjoen 1980, Milgram 1983, Hugi 1993) are also plotted together for comparison. The data indicate the dependence of entrainment coefficient on the height from the source, initial buoyancy flux, and slip velocity. As shown in the graph, the entrainment coefficient decreases as the plume rises. Likewise, the higher the bubble flow rate, the larger the entrainment coefficient. This collapse of the data shows that the slip velocity together with the buoyancy flux and plume height can influence the entrainment in a simple bubble plume.

SUMMARY AND CONCLUSIONS

The PTV and PIV methods have been applied to obtain full-field velocity information in an unbounded air bubble plume in a quiescent, unstratified ambient condition. To keep the experiments and post-processing as simple as possible, a new phase separation method has been proposed. Mixed-fluid images are obtained during the experiments. Because the bubble phase reflects brighter than the PIV tracer particles, a gray-scale intensity threshold is applied to obtain images that contain the bubble signature only. These images are processed using the standard PTV method and then time-averaged to obtain the average velocity field data for the bubbles. The raw images are simultaneously processed using the standard PIV technique, resulting in vector maps containing the bubble and entrained fluid signatures. A maximum velocity threshold and vector median filter is applied to remove the bubble vectors; the parameters of the median filter are adjusted to give a match between the extracted bubble vectors from the PIV and the PTV data of the bubbles only. The remaining PIV vectors are interpreted to be the velocity field of the entrained ambient fluid. More detailed phase separation methods are availabe in the literature. However, this method is shown to be adequate for obtaining mean flow properties and is inexpensive, simplifying the task of phase separation, because it relies only on standard PIV and PTV functions available in most software packages.

From the phase separated velocity data, time-averaged results are obtained. The entrained fluid velocity data match well with the Gaussian profile, while the bubble velocity data match closer to a top-hat profile. By fitting Gaussian profiles to the entrained fluid data, results are obtained for the centerline velocity, plume width, entrained fluid volume flux and dispersed phase void fraction. These data are integrated to give a measurement of the bubble-plume entrainment coefficient as a function of height.

The important conclusions from these data are summarized as follows:

1. Time average results for the entrained ambient fluid of the centerline velocity, plume

width, and volume flux can be non-dimensionalized using the governing parameters B and z to achieve a good collapse of the data. This indicates that the slip velocity of the bubbles do not significantly affect these variables.

2. The entrainment coefficient evaluated from these data shows a significant dependence on slip velocity and height above the diffuser, likely due to variation in void fraction. This supports the understanding that a bubble plume is not self-similar.

3. By comparison to entrainment coefficient data from other researchers, there appears to be a minimum value of the entrainment coefficient in a bubble plume of around 0.04. This invalidates the dependence of the entrainment coefficient on the bubble Froude number as proposed by Milgram (1983) for bubble Froude number below about 2.

4. A new correlation of the entrainment coefficient in a simple bubble plume has been proposed that is a function of the non-dimensional slip velocity $u_s/(B/z)^{1/3}$ which is the cube of the ratio of the slip velocity to a characteristic velocity in the plume. Hence, entrainment depends on the relative velocity of the bubbles as compared to the velocity of the entrained ambient fluid.

ACKNOWLEDGEMENT

This paper is based upon work supported by the National Science Foundation under Grant No. CTS-0348572 and by the German Academic Exchange Service Grant No. DAAD 315 D/03/41981.

REFERENCES

Asaeda, T. & Imberger, J. (1993), 'Structure of bubble plumes in linearly stratified environments', *J. Fluid Mech.* **249**, 35–57.

Brücker, C. (2000), *PIV in two-phase flows*, Lecture series 2000-01, Von Karman Institute for Fluid Dynamics, Rhode-Saint-Genese, Belgium.

Caulfield, J. A., Adams, E. E., Auerbach, D. I. & Herzog, H. J. (1997), 'Impacts of ocean CO_2 disposal on marine life: II. Probabilistic plume exposure model used with a time-varying dose-response analysis', *Env. Model. and Assess.* **2**(4), 345–353.

Deen, N. (2001), An experimental and computational study of fluid dynamics in gas-liquid chemical reactors, PhD thesis, Aalborg University, Esbjerg, Denmark.

Deen, N., Westerweel, J. & Delnoij, E. (2002), 'Two-phase PIV in bubbly flows: status and trends', *Chem. Eng. Technol.* **25**(1), 97–101.

Delnoij, E., Westerweel, J., Deen, N., Kuipers, J. & van Swaaij, W. (1999), 'Ensemble correlation PIV applied to bubble plumes rising in a bubble column', *Chem. Eng. Sci.* **54**, 5159–5171.

Fenneløp, T. & Sjoen, K. (1980), Hydrodynamics of underwater blowouts, *in* 'Proc. of AIAA 18th Aerospace Sci. Meeting', Pasadena, CA.

Fischer, H. B., List, E. G., Koh, R. C. Y., Imberger, J. & Brooks, N. H. (1979), *Mixing in Inland and Coastal Waters*, Academic Press, New York, NY.

Grota, B. & Strauß, K. (2000), DPIV in a particle-laden gas flow - the influence of the particle fluctuation velocities on the accuracy of several cross-correlation-based analysis methods, *in* 'EUROMECH 4', Eindhoven, The Netherlands.

Gui, L., Lindken, R. & Merzkirch, W. (1997), Phase-separated PIV measurements of the flow around systems of bubbles rising in water, ASME fluids engineering division summer meeting, Vancouver, BC, Canada.

Gui, L. & Merzkirch, W. (1996), 'A method of tracking ensembles of particle images', *Exp. Fluids* **21**(6), 465–468.

Hilgers, S., Merzkirch, W. & Wagner, T. (1995), 'PIV measurements in multiphase flow using CCD-and Photo-camera', *ASME FED* **209**, 151–154.

Hugi, C. (1993), Modelluntersuchungen von Blasenstrahlen für die Seebelüftung, Ph.D. Thesis, Inst. f. Hydromechanik u. Wasserwirtschaft, ETH, Zürich.

Kiger, K. & Pan, C. (2000), 'PIV technique for the simultaneous measurement of dilute two-phase flows', *J. Fluids. Engrg.* **122**(4), 811–818.

Kobus, H. E. (1968), Analysis of the flow induced by air-bubble systems, *in* 'Proc. 11th Int. Conf. Coastal Engrg., London', ASCE, Reston, VA, pp. 1016–1031.

LaVision GmbH (2002), *DaVis FlowMaster Software Mannual for DaVis 6.2*, LaVision GmbH, Goettingen, Germany.

Lemckert, C. J. & Imberger, J. (1993), 'Energetic bubble plumes in arbitrary stratification', *J. Hydr. Engrg.* **119**(6), 680–703.

Lindken, R., Gui, L. & Merzkirch, W. (1999), ‘Velocity measurements in multiphase flow by means of particle image velocimetry’, *Chem. Eng. Technol.* **22**(3), 202–206.

Lindken, R. & Merzkirch, W. (2002), ‘A novel PIV technique for measurements in multiphase flows and its application to two-phase bubbly flows’, *Exp. Fluids* **33**(6), 814–825.

McDougall, T. J. (1978), ‘Bubble plumes in stratified environments’, *J. Fluid Mech.* **85**(4), 655–672.

Milgram, J. H. (1983), ‘Mean flow in round bubble plumes’, *J. Fluid Mech.* **133**, 345–376.

Monkewitz, P. A. (1988), ‘The absolute and convetive nature of instability in two-dimensional wakes at low reynolds numbers’, *Phys. Fluids* **31**(5), 999–1006.

Motarjemi, M. & Jameson, G. (1978), ‘Mass transfer from very small bubbles - the optimum bubble size for aeration’, *Chem. Eng. Sci.* **33**(11), 1415–1423.

Oakley, T., Loth, E. & Adrain, R. (1997), ‘A two-phase cinematic PIV method for bubbly flows’, *J. Fluids. Engrg.* **119**(3), 707–712.

Raffel, M., Willert, C. E. & Kompenhans, J. (1998), *Particle image velocimetry: A practical guide*, Experimental Fluid Mechanics, Springer Velag, New York.

Sakakibara, J., Wicker, R. & Eaton, J. (1996), ‘Measurements of particle-fluid velocity correlation and the extra dissipation in a round jet’, *J. Multiphase Flow* **22**(5), 863–881.

Schlüter, M. & Räbiger, N. (1998), Bubble swarm velocity in two-phase flows, *in* ‘Proceedings of the ASME Heat Transfer Division’, Vol. 361-5, pp. 275–280.

Socolofsky, S. A. (2001), Laboratory Experiments of Multi-phase Plumes in Stratification and Crossflow, Ph.D. Thesis, Dept. of Civ. Env. Engrg., MIT, Cambridge, MA.

Socolofsky, S. A. & Adams, E. E. (2002), 'Multi-phase plumes in uniform and stratified crossflow', *J. Hydr. Res.* **40**(6), 661–672.

Socolofsky, S. A. & Adams, E. E. (2003), 'Liquid volume fluxes in stratified multiphase plumes', *J. Hydr. Engrg.* **129**(11), 905–914.

Socolofsky, S. A. & Adams, E. E. (2005), 'Role of slip velocity in the behavior of stratified multiphase plumes', *J. Hydr. Engrg.* **131**(4).

Socolofsky, S. A., Crounse, B. C. & Adams, E. E. (2002), Multi-phase plumes in uniform, stratified and flowing environments, *in* H. Shen, A. Cheng, K.-H. Wang, M. H. Teng & C. Liu, eds, 'Environmental Fluid Mechanics–Theories and Applications', ASCE/Fluids Committee, chapter 4, pp. 84–125.

Sridhar, G., Ran, B. & Katz, J. (1991), Implementation of particle image velocimetry to multi-phase flow, *in* 'Cavitation Multiphase Flow Forum', ASME, New York, pp. 205–210.

Westerweel, J. (1994), 'Efficient detection of supurious vectors in particle image velocimetry data', *Exp. Fluids* **16**(3-4), 236–247.

Wüest, A., Brooks, N. H. & Imboden, D. M. (1992), 'Bubble plume modeling for lake restoration', *Water Resour. Res.* **28**(12), 3235–3250.

Yapa, P. D., Zheng, L. & Nakata, K. (1999), ‘Modeling underwater oil/gas jets and plumes’, *J. Hydr. Engrg.* **125**(5), 481–491.

LIST OF FIGURES

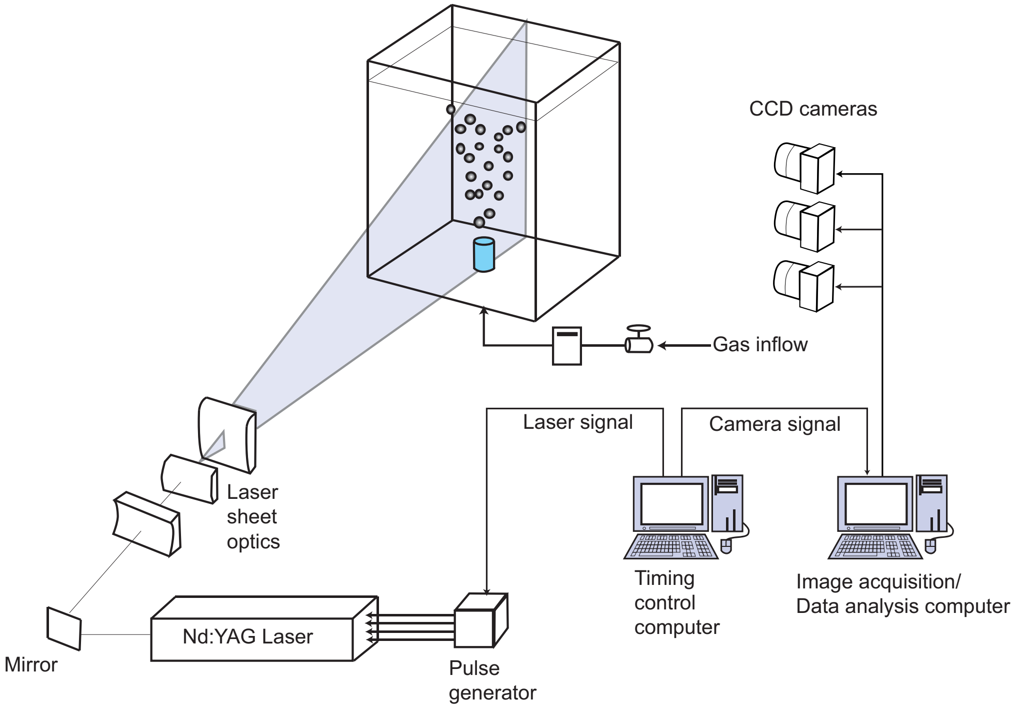

FIG. 1: Laboratory experimental setup for the PIV and PTV methods.

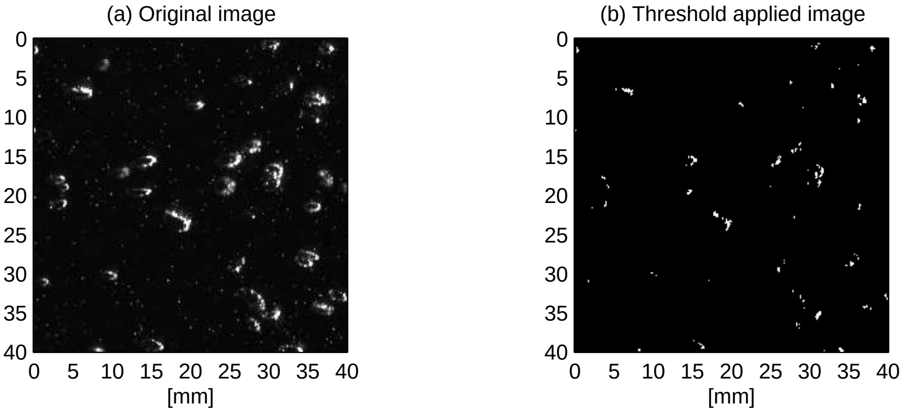

FIG. 2: PTV image processing: (a) raw image of the mixed fluid phases and (b) image containing bubbles only, obtained by applying a threshold filter to image (a).

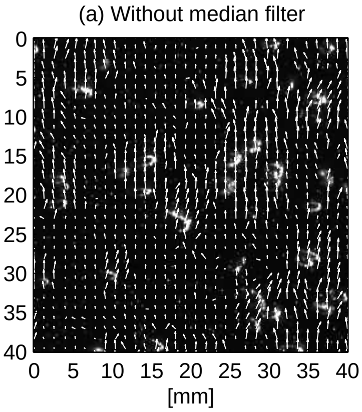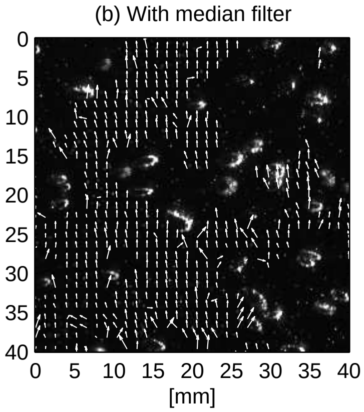

FIG. 3: Raw velocity vector map (a) and median filtered velocity vector map (b).

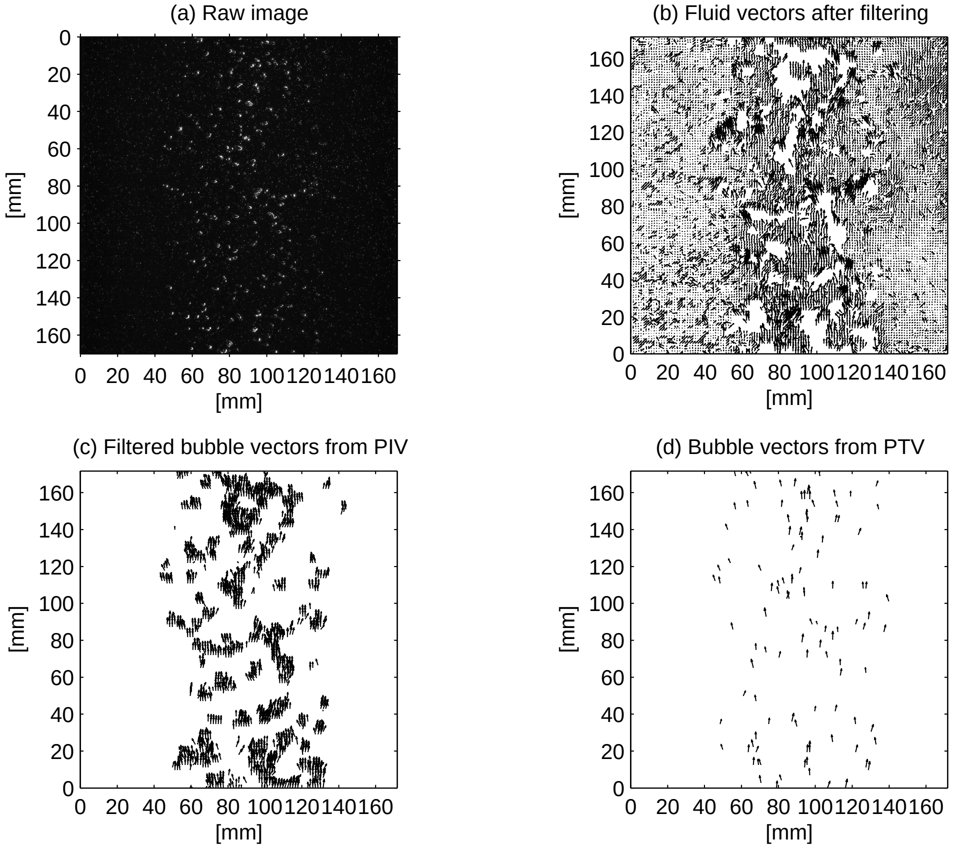

FIG. 4: Example of the phase separation method and the results of the PIV and PTV analysis.

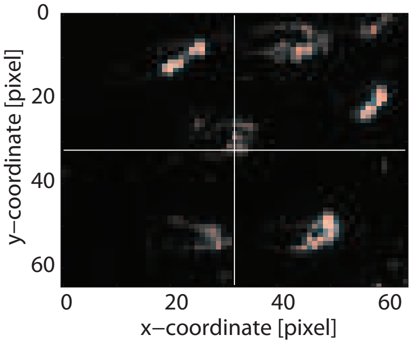

FIG. 5: Sample view of four 32×32-pixel interrogation windows showing the relative size of bubbles and entrained fluid tracer particles.

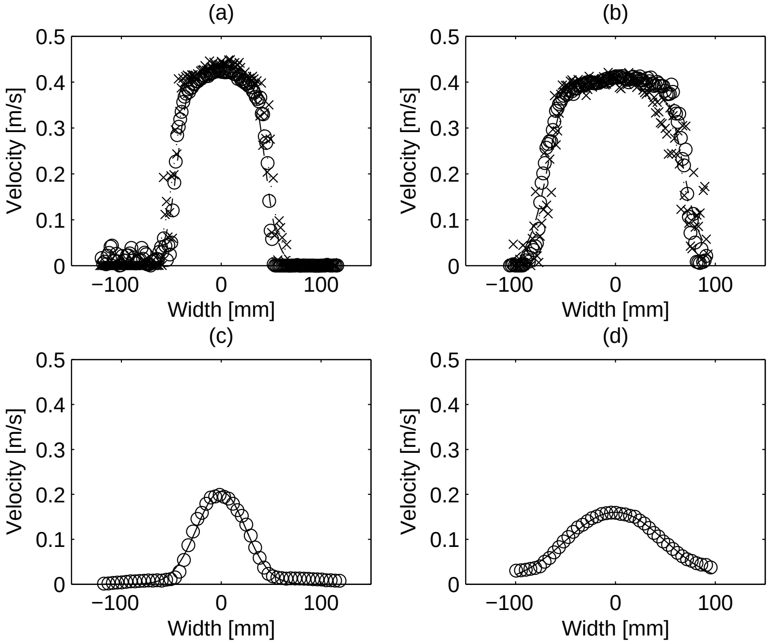

FIG. 6: Velocity profiles for the bubble phase (a and b) and the entrained fluid phase (c and d). Symbols denote measured data from the PIV (○) and PTV (×) analysis and lines present the fitted Monkewitz (a and b) and Gaussian (c and d) curves.

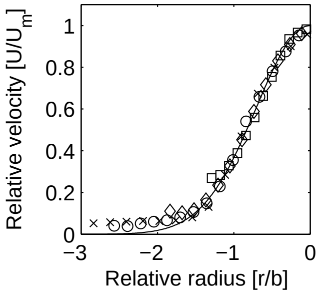

FIG. 7: Normalized fluid phase velocity at $z = 100$ mm($\circ$), $z = 200$ mm($\times$), $z = 350$ mm($\Diamond$), $z = 500$ mm($\Box$).

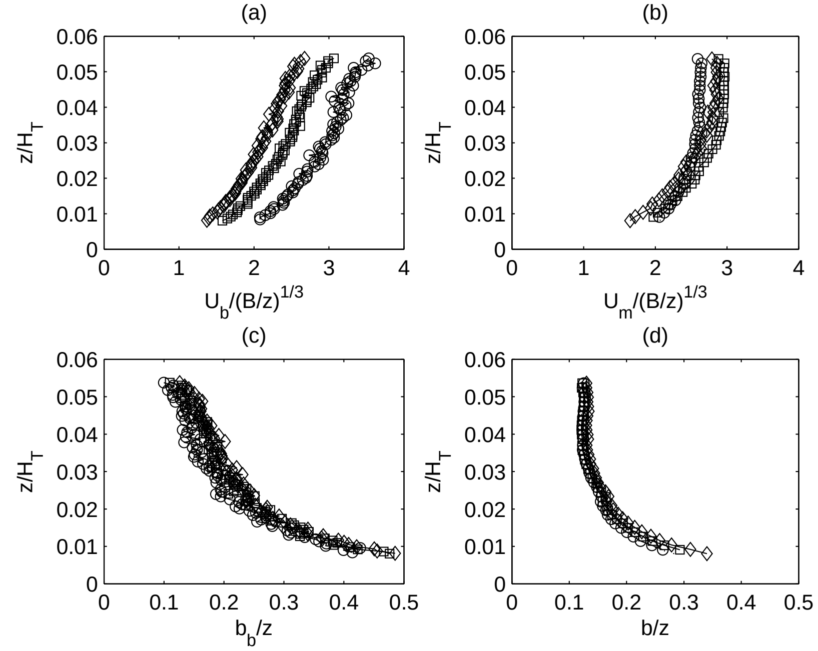

FIG. 8: Centerline velocity for the bubble phase (a) and entrained fluid phase (b) and plume width for the bubble phase (c) and the entrained fluid phase (d) for bubble flow rates of 0.5 l/min (○), 1.0 l/min (□), 1.5 l/min (◇).

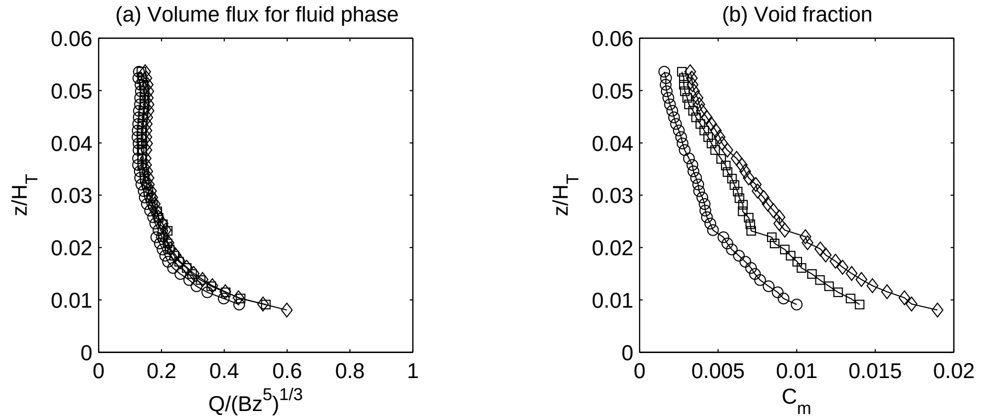

FIG. 9: Calculated entrained fluid flow rate (a) and void fraction (b) for bubble flow rates of 0.5 l/min (○), 1.0 l/min (□), 1.5 l/min (◇).

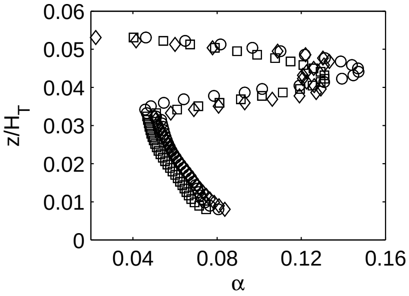

FIG. 10: The entrainment coefficient as a function of non-dimensional height for bubble flow rates of 0.5 l/min (○), 1.0 l/min (□), 1.5 l/min (◇).

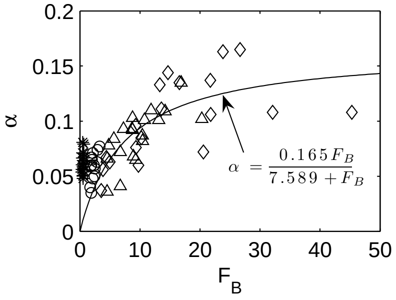

FIG. 11: Dependence of the plume entrainment coefficient on the bubble Froude number. Data from the present study are depicted by $*$. Other symbols present Kobus (1968) ($\circ$), Fennelop & Sjoen (1980) ($\triangle$), and Milgram (1983) ($\diamondsuit$).

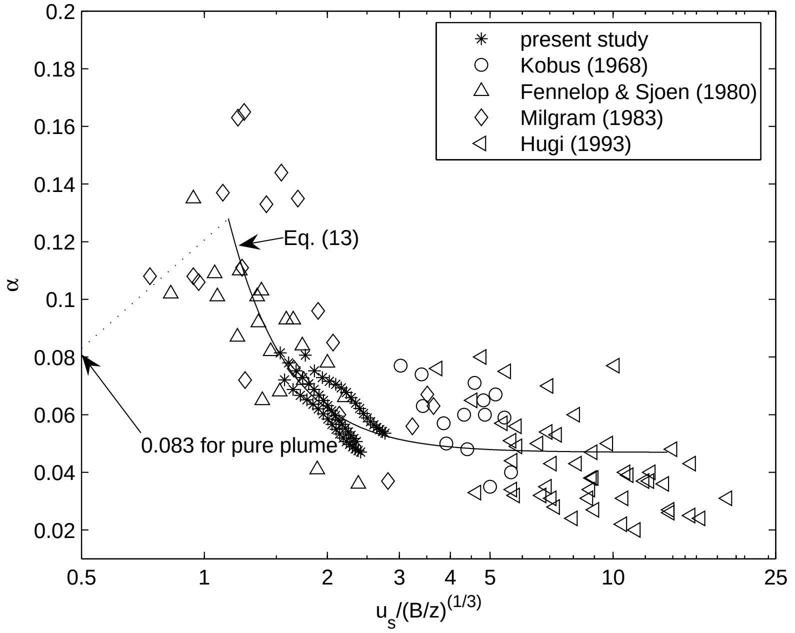

FIG. 12: The entrainment coefficient as a function of $u_s/(B/z)^{1/3}$.